The International Journal of Advanced Manufacturing Technology (2021) 115:3713–3729
https://doi.org/10.1007/s00170-021-07409-4

ORIGINAL ARTICLE

Comparative analysis of the machining temperatures of an end mill and a novel tool in the orbital drilling of CFRP composites

Linghao Kong[1] · Dong Gao[1] · Yong Lu[1]

Received: 28 January 2021 / Accepted: 2 June 2021 / Published online: 9 June 2021
© The Author(s), under exclusive licence to Springer-Verlag London Ltd., part of Springer Nature 2021

Abstract

The defects and rejections caused by the combined action of thrust force and cutting heat impede the wide application of carbon fiber-reinforced plastic (CFRP). To study the cutting temperature of two kinds of tools in the orbital drilling of CFRPs, a cutting force model and a heat transfer model were proposed in this research. The three-dimensional heat transfer equation in polar coordinates was established to predict the temperature inside the workpiece and was solved with the finite difference approach. The cutting edge on the bottom of the tool is the main cause of the thrust force, and due to the accumulation of cutting heat, the processing temperature at the exit is higher. The results show that the predictions of the model coincide with the experimental data and that the model can predict the temperature field inside the workpiece in the process of orbital drilling. The novel orbital drilling and reaming tool can effectively reduce the processing temperature of orbital drilling.

Keywords Orbital drilling · Machining temperature · CFRP · Cutting tool · Temperature distribution model

Nomenclature

a_p	Screw pitch of the helical path
e	Eccentricity of the helical path
d	Diameter of the milling part
f_t	Tangential feed rate
f_z	Feed rate in the z-direction
D	Diameter of the peripheral cutting edges
F	Cutting force of the ODR tool
F_M	Cutting force generated by the milling part
F_R	Cutting force generated by the reaming part
F_P	Cutting force generated by the peripheral cutting edges
n_t	Spindle rotation speed
n_h	Orbital rotation speed
K_{Mac}, K_{Mae}	Force coefficients related to the milling part
r_t	Radius of the milling part
θ_t	Angular position of the tool coordinates to the workpiece coordinates
θ_0	Initial angular position in the tool coordinates
ω_h	Angular velocity of the orbital rotation
φ_{e1}	Angular position of the 1st cutting edge
φ_0	Initial angular position of the 1st cutting edge
N	Number of cutting edges on the tool
ω	Angular velocity of the spindle rotation
φ_e	Angle between two adjacent cutting edges
j	jth cutting edge of the tool
φ_{ej}	Angular position of the jth cutting edge
$\varphi_j(t, z)$	Angular position of the jth cutting edge with a height of z at time t
ds	Length of a cutting element
dz	Height of a cutting element
z	Height of the cutting edge element
β	Helix angle of the end mill
$h_j(\varphi_j, z)$	Thickness of chip at an angle of φ_j and height of z
H	Height of the reaming part

✉ Yong Lu
luyong@hit.edu.cn

Linghao Kong
linghao8959@163.com

Dong Gao
gaodong@hit.edu.cn

[1] School of Mechatronics Engineering, Harbin Institute of Technology, Harbin, China

R_z	Radius of the reaming part at a height of z
$dF_{xj}^{tR}, dF_{yj}^{tR}, dF_{zj}^{tR}$	Cutting forces in the x-, y-, and z-directions of a cutting edge element on the reaming part in the cutter coordinates
$F_{xj}^{tR}, F_{yj}^{tR}, F_{zj}^{tR}$	Cutting forces in the x-, y-, and z-directions of the reaming part in the cutter coordinates
$F_{xj}^{tP}, F_{yj}^{tP}, F_{zj}^{tP}$	Cutting forces in the x-, y-, and z-directions of the peripheral cutting edges in the cutter coordinates
F_x^t, F_y^t, F_z^t	Cutting forces of the ODR tool in the x-, y-, and z-directions in the tool coordinates
F_x^w, F_y^w, F_z^w	Cutting force of the ODR tool in the x-, y-, and z-directions in the workpiece coordinates
$\dot{Q}_{fs}(\varphi)$	Heat generated on the shear plane in the first deformation zone of a cutting element
F_s	Shearing force of a cutting element
v_s	Shear velocity
$\dot{Q}_{fsw}$	Heat $\dot{Q}_{fs}(\varphi)$ transfer to the workpiece
K_w	Thermal diffusivity of the workpiece
ϕ_n	Shear angle
γ_n	Front rake angle
$\dot{Q}_{tf}(\varphi)$	Heat generated due to friction in the third deformation zone of a cutting element
$F_f(\varphi)$	Force of the friction of a cutting element
$\dot{Q}_{tfw}$	Heat $\dot{Q}_{tf}(\varphi)$ transfer to the workpiece
b	Cutting width
l_{wf}	Length of the furrow area
$\lambda_1, \lambda_2, \lambda_3$	Heat conductivity of the CFRP in the x-, y-, and z-directions
$r_w\theta_w z_w$	Radius, angle and height of the node position
T	Temperature of the workpiece
T_0	Ambient temperature
ρ	Density of the workpiece
c	Heat capacity of the workpiece
h	Convective heat transfer coefficient
$q(r, \theta, z, t)$	Heat flux generated by the heat source

1 Introduction

With excellent mechanical and physical properties, such as high strength and light weight, carbon fiber-reinforced plastic (CFRP) has been widely applied in the aviation and aerospace fields. Because the CFRP parts are structural components and skins, a substantial number of rivets and bolts with high dimensional tolerance and surface quality need to be drilled in these parts [1] for connections. However, unsatisfactory machining quality still restricts the reliability of CFRP parts. CFRP is a laminated structure generally composed of carbon fiber cloth and resin. Carbon fiber has high strength and high-temperature resistance, while the resin is sensitive to temperature. The elastic modulus and strength plummet when the temperature exceeds the glass transition temperature (150–250 °C) [2]. A CFRP workpiece has low thermal conductivity and specific heat capacity, and heat accumulation during machining leads to an apparent temperature increase around the cutting area. The insufficient interlaminar shear strength and transverse tensile strength of CFRP are more influential with the impact of the processing temperature [3]. Many severe machining defects are generated due to this deficiency, such as burring and fuzzing, fiber pull out, matrix cracking, and delamination. In particular, delamination is judged to be the most catastrophic defect because it leads to rapid declines in the stiffness and carrying capacity of the mechanical components. Thus, the study of the magnitude and distribution of CFRP workpiece temperatures during processing should be of great significance.

To improve the drilling quality of CFRP components, the effects of the tool performance and cutting parameters on the damage of CFRP holes have been widely studied in recent decades. The effects of the drill types (twist drill [4–6], candlestick drill [6, 7], step drill [8, 9], core drill [10, 11], etc.), tool geometry (diameter [12, 13], point angle [14], and chisel length [15]), and tool material [15, 16] on the machining quality were studied. Although drill bits with special structures can achieve superior processing quality, sometimes high quality, high efficiency, low cost, and other industry requirements are still difficult to satisfy. Orbital drilling [17, 18], wobble milling [19, 20], vibration-assisted cutting [21], water jet cutting [22], laser cutting [23], and EDM [24] have also been used to improve the drilling quality of CFRP components. Among the methods mentioned, orbital drilling has been widely adopted in practice. In this method, the end mill rotates around the tool axis, which is parallel to the hole axis, making a planetary motion around the hole axis at the same time [25]. Orbital drilling has many advantages over traditional drilling, including a longer tool life, a lower cutting temperature, and a lower thrust force that contribute to effectively reducing the possibility of delamination [17, 26]. Based on the comprehensive consideration of the machining quality, cost, and efficiency, orbital drilling is the most promising machining method for CFRP drilling. To further improve the quality of orbital drilling, tilted helical milling [25], tilted orbital grinding [1], and two-step techniques [27] have also been proposed.

To clarify the temperature field inside the workpiece and the tool, the mechanisms of heat generation and heat distribution in the cutting process have been studied over a long time. The cutting temperature in metal cutting was studied as early as 1907, and Taylor and Fred [28] revealed the effect of cutting speed on the cutting temperature and tool life. In early

studies on cutting temperature, data were obtained mainly by experimental measurements, such as thermocouple measurements, infrared imaging, and thermocolor measurements. These experimental measurements are not reusable, time consuming, and costly. Therefore, numerical and analytical models have been proposed, widely considered, and used until now. Based on the moving heat source model in the 1940s, a prototype of the cutting temperature model was established. After years of research, analytical models have the ability to predict the magnitude and distribution of workpiece temperatures and have been applied to many engineering fields. To more accurately predict the cutting temperature, Komanduri and Hou [29–31] studied the heat generated in the shear plane and tool-chip interface in the cutting process and calculated the temperature field distribution at the tool-chip interface. By discretizing the cutting edge and the time history into microelements, they simplified the tool movement, and then a model was established by Lin et al. [32] to predict the cutting temperature of the workpiece during the end milling process that took into consideration the wear of the flank face. The accuracy of the model is higher than that of the analytical model, and the prediction efficiency is higher than that of the finite element method, which can be used to optimize the cutting parameters. Based on the nonuniform heat distribution ratio along the interface of the primary and second heat sources, Huang and Liang [33] proposed a new model with better matching and prediction accuracy for analyzing the cutting temperature. With the development of calculation methods and improvement in the calculation capacity, the finite element method (FEM) has been widely used in the calculation of cutting temperature [34–36]. The FEM is time consuming, and the accuracy of the material's constitutive properties has a significant influence on the accuracy of the prediction. In the 1960s, Dutt and Brewer [37] solved differential heat transfer equations with the finite difference method and obtained an excellent prediction effect. With the enhancement in computing power, the finite difference method can be used to solve differential equations with high efficiency and accuracy. Lazoglu and Altintas [38] presented a numerical model that predicts the temperature fields in the tool and chip in a time-varying milling process. Liu et al. [39, 40] solved a three-dimensional heat transfer model describing the temperature field of the workpiece during helical milling by the Green function approach. Zhang et al. [41] took a large number of exit temperatures of CFRP drilling obtained by experimental measurement as the training object and established a prediction model of CFRP drilling exit temperature with a neural network.

Cutting temperatures in machining significantly impact the tool life, size and shape tolerances, and residual stress in the machined part. Several scholars have studied approaches for reducing the cutting temperature. Through the application of semiartificial thermocouples, Sun et al. [42] found that the cutting temperature showed a similar upward trend with increasing cutting parameters. To optimize the tool life, Sheng et al. [43] proposed a modeling coupling equation of cutting parameters based on the optimal cutting temperature. Wang et al. [44] studied the relationship between the cutting parameters, cutting temperature, and cutting force in CFRP milling with RSM and pointed out that cutting speed has a significant influence on the cutting temperature. Research on the cutting temperature in drilling thermoplastic polymers by Weinert et al. [45] showed that a low cutting speed and high feeds are helpful for realizing optimal tool temperature and for reducing the heat impact zone. Guimaraes et al. [46] improved the thermal conductivity of a tool by incorporating copper heat sinks at a designated position in the tool. Sasahara et al. [47] studied the effect of MQL on the cutting temperature in driven rotary cutting, and the results showed that the rotation of the tool and MQL can reduce the cutting temperature and decrease tool wear. Most of the studies on reducing the temperature of the machined area focus on the optimization of the cutting parameters, the use of improved tools, and the use of coolants.

CFRP materials are far less widely used than metal materials, and most of the research on the cutting heat of CFRP is conducted with experimental measurement methods, such as the use of thermocouples [2], infrared imaging [41, 48, 49], and fiber Bragg gratings [50]. The processing temperature has an important influence on the quality of CFRP drilling. However, the use of conventional cutting compounds has an effect on the strength of the CFRP workpiece, while the usage of cryogenic gas for cooling causes powdery chips to float in the air, posing a threat to the environment and operator health. Therefore, research on the temperature field distribution of CFRP workpieces during processing and ways to reduce the processing temperature are scarcely reported.

Orbital drilling is considered to be the most promising method of CFRP drilling. In a previous study, utilizing an orbital drilling and reaming (ODR) tool [51] can further improve the processing quality, prolong the tool life, and reduce the processing temperature without changing the processing equipment of orbital drilling, which has good prospects for application. To further study the machining performance of an end mill and ODR tool, a numerical model revealing the magnitude and distribution of workpiece temperatures that considers the influence of convective heat transfer on the cutting temperature is proposed in this paper. Taking the different thermal diffusivities of CFRP in different directions into account, a three-dimensional, unsteady state, nonhomogeneous partial differential heat transfer equation in polar coordinates was established. The finite difference approach was used to solve the heat transfer equation. The heat fluxes of the two kinds of tools in processing were calculated. The temperature changes inside the workpiece of the two kinds of cutting tools during machining were calculated and compared with the

experimental results. The experimental results were in good agreement with the prediction model. This study verified that the ODR tool in orbital drilling can reduce the cutting temperature in machining. Section 2 presents the process of machining temperature prediction. The experimental instruments and cutting parameters used in this research are recorded in Section 3. The experimental results are analyzed in Section 4, and the conclusion is drawn in the last section.

2 Machining temperature of the end mill and ODR tool in orbital drilling

2.1 Processing with ODR tool

Orbital drilling (helical milling) is a hole processing technique that involves eccentric milling with an end mill. The ODR tool is a dedicated tool for orbital drilling, and the processing presents a novel material removal process that is different from that of conventional orbital drilling (COD). Figure 1 shows an ODR tool and hole processing with the ODR tool, where Fig.1a is the ODR tool and Fig. 1b–d show the exit formation of the ODR tool. The ODR tool consists of three parts: a milling part with a diameter of d, peripheral cutting edges with a diameter of D, and a reaming part with a varied diameter that connects the peripheral cutting edges to the milling part. The hole made by the milling part has a smaller diameter than the requirement. The reaming part is used to expand the hole made by the milling part. Taking the material at the exit as an example, the tool moves along the axis of the tool, and the milling part of the ODR tool touches the bottom of the workpiece first, producing a hole with a diameter of d. Regarding the impact of the combined effect of the spiral trajectory and the reaming part, the size of the exit is expanded continuously, and the size is enlarged to the required size until the reaming part completely passes through the workpiece.

2.2 Temperature field prediction of the workpiece in processing

2.2.1 Analysis of the cutting force in orbital drilling

To calculate the temperature distribution inside the workpiece, the cutting force model of orbital drilling should be established to calculate the heat generated in the cutting process first. Owing to the shape of the ODR tool, the cutting force of the ODR tool in orbital drilling is more complicated than that of an end mill. Therefore, this paper takes the ODR tool as an example to model the cutting force of orbital drilling.

The ODR tool is composed of the milling part, the reaming part, and the peripheral cutting edges, all of which participate in cutting during machining. Therefore, the model includes the influence of three parts on the cutting force, and the cutting force can be formulated as

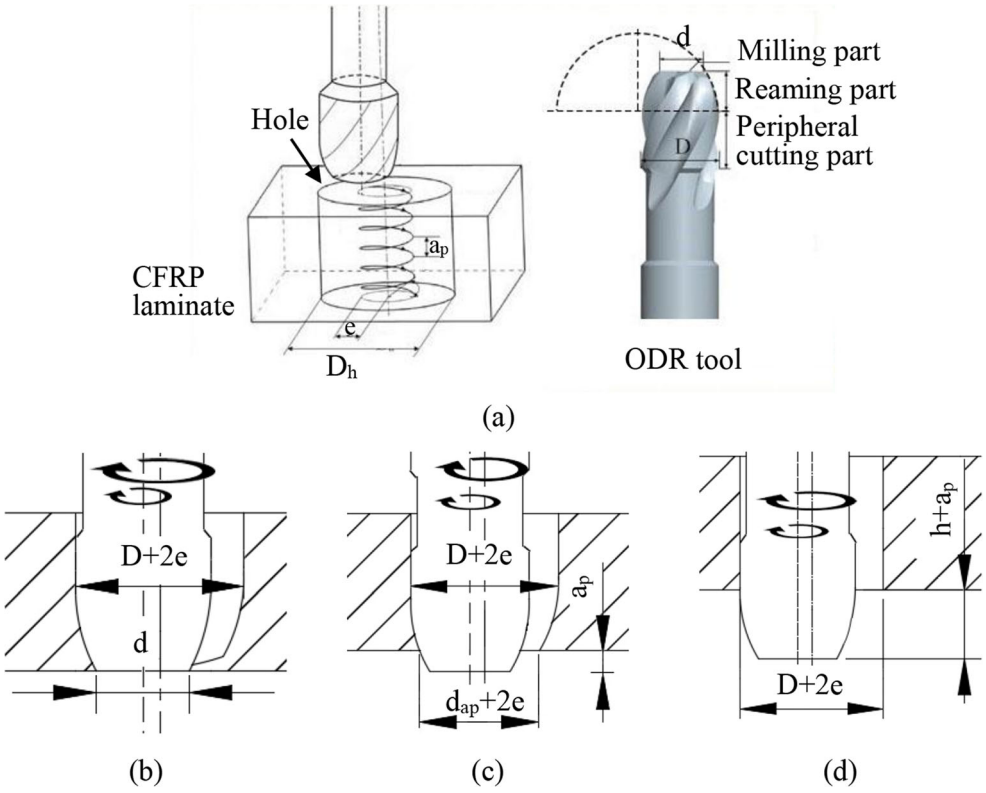

Fig. 1 ODR tool and hole processing with the ODR tool: **a** ODR tool, **b**–**d** exit formation of the ODR tool

$$F(t) = F_M(t) + F_R(t) + F_P(t) \tag{1}$$

The spindle rotation speed n_t is far greater than the orbital rotation speed n_h in orbital drilling. Therefore, the influence of the milling part due to orbital rotation on the cutting force is ignored. Assuming that the milling part only produces the cutting force along the tool axis, this force can be expressed by the cutting force coefficient, cutting width, and chip thickness as

$$F_M = (K_{Mac} h_{za} + K_{Mae}) r_t \tag{2}$$

The modeling processes of the reaming part and peripheral cutting edges are similar; the reaming part is taken as an example. The cutter coordinates $O_t X_t Y_t Z_t$ are established with the center of the milling part as the origin, and the workpiece coordinates $O_w X_w Y_w Z_w$ are established with the center of the hole as the origin. The position of the tool and the cutting edge is shown in Fig. 2a and can be calculated by Eq. (7).

$$\theta_t(t) = \theta_0 + \omega_h t \tag{3}$$

$$\varphi_{e1} = \varphi_0 + \omega t \tag{4}$$

$$\varphi_e = 2\pi / N \tag{5}$$

$$\varphi_{ej} = \varphi_{e1} + (j-1)\varphi_e \tag{6}$$

$$\varphi_j(t,z) = \varphi_{ej} + \frac{z \cdot \tan\beta}{R} \tag{7}$$

The undeformed chip geometry in orbital drilling with the ODR tool is shown in Fig. 2b and c. The tool contains N cutting edges. The jth cutting edge of the reaming part is divided into many tiny cutting edges, where each element has a height of dz and a length of ds.

$$ds = dz / \cos\beta \tag{8}$$

The cutting edge element is taken as the origin, the movement direction of the element is taken as the Y-axis, the direction pointing to the tool axis is taken as the X-axis, and the vertical direction is taken as the Z-axis to establish the element coordinates. Then, the tangential force (dF_{tj}), the radial force (dF_{rj}) and the axial force (dF_{aj}) of each cutting edge element can be expressed as

$$\begin{cases} dF_{tj} = K_{tc} h_j\left(\varphi_j, z\right) dz + K_{te} ds \\ dF_{rj} = K_{rc} h_j\left(\varphi_j, z\right) dz + K_{re} ds \\ dF_{aj} = K_{ac} h_j\left(\varphi_j, z\right) dz + K_{ae} ds \end{cases} \tag{9}$$

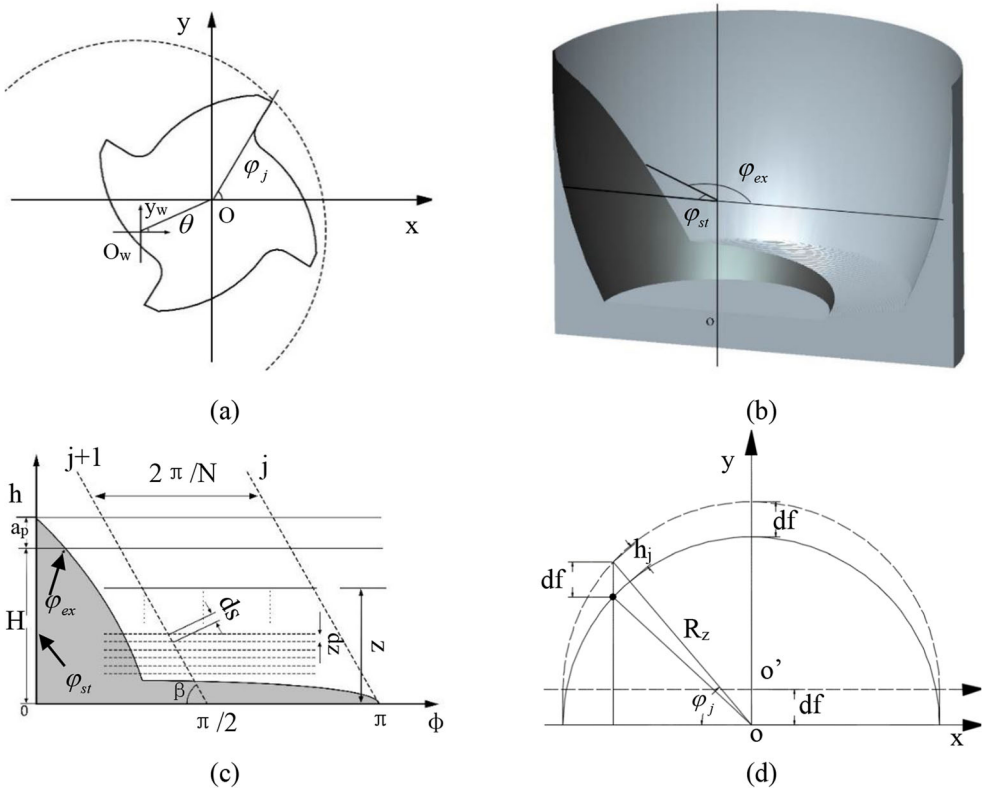

Fig. 2 Illustration of orbital drilling with the ODR tool: **a** the tool coordinates and workpiece coordinates, **b** the undeformed chip geometry in orbital drilling with the ODR tool, **c** an illustration of the cutting element, and **d** the undeformed chip thickness

where φ_j is the instantaneous immersion angle of the cutting edge element, $h_j(\varphi, z)$ is the thickness of chip at an angle of φ_j a height of z, and K_{tc}, K_{te}, K_{rc}, K_{re}, K_{ac}, and K_{ae} are the cutting force coefficients calibrated by experiments. As illustrated in Fig. 2d, the edges move *df* along the y-axis in the tool coordinates, and the thickness of the undeformed chip is related to the angle position of the cutting edge element. Then, $h_j(\varphi, z)$ can be calculated by Eq. (10).

$$h_j\left(\varphi_j, z\right) = \sqrt{\left(R_z \cdot \sin\varphi_j + df\right)^2 + \left(R_z \cdot \cos\varphi_j\right)^2} - R_z \quad (10)$$

As Fig. 2b and c show, the edges cut into the workpiece at φ_{st} and cut out at φ_{ex}. Then, the function $g(\varphi_j)$ is established to estimate whether the cutting element involves processing.

$$g\left(\varphi_j\right) = \begin{cases} 1 & \varphi_{st} \le \varphi_j \le \varphi_{ex} \\ 0 & \varphi_j < \varphi_{st} \ or \ \varphi_{ex} < \varphi_j \end{cases} \quad (11)$$

Then, Eq. (9) can be rewritten as,

$$\begin{cases} dF_{tj} = g\left(\varphi_j\right)\left(K_{tc} h_j\left(\varphi_j, z\right) dz + K_{te} ds\right) \\ dF_{rj} = g\left(\varphi_j\right)\left(K_{rc} h_j\left(\varphi_j, z\right) dz + K_{re} ds\right) \\ dF_{aj} = g\left(\varphi_j\right)\left(K_{ac} h_j\left(\varphi_j, z\right) dz + K_{ae} ds\right) \end{cases} \quad (12)$$

The element coordinates distributed on the surface of the reaming part are transformed to the cutter coordinates $O_t X_t Y_t Z_t$, and the cutting force of a cutting edge element can be obtained as

$$\begin{cases} dF_{xj}^{tR} = -\cos\left(\varphi_j\right) \cdot dF_{tj} - \sin\left(\varphi_j\right) \cdot dF_{rj} \\ dF_{yj}^{tR} = \sin\left(\varphi_j\right) \cdot dF_{tj} - \cos\left(\varphi_j\right) \cdot dF_{rj} \\ dF_{zj}^{tR} = dF_{aj} \end{cases} \quad (13)$$

The cutting force of the reaming part in the tool coordinates can be calculated by integrating the element cutting force on all cutting edges along the tool axis.

$$\begin{cases} F_x^{tR} = \sum_{j=1}^{N} \int_0^H \left(-\cos\left(\varphi_j\right) \cdot dF_{tj} - \sin\left(\varphi_j\right) \cdot dF_{rj}\right) dz \\ F_y^{tR} = \sum_{j=1}^{N} \int_0^H \left(\sin\left(\varphi_j\right) \cdot dF_{tj} - \cos\left(\varphi_j\right) \cdot dF_{rj}\right) dz \\ F_z^{tR} = \sum_{j=1}^{N} \int_0^H dF_{aj} dz \end{cases} \quad (14)$$

Through the modeling of the cutting force of the peripheral cutting edges with the same method, the cutting force of the ODR tool is expressed as follows:

$$\begin{cases} F_x^t = F_{xj}^{tR} + F_{xj}^{tP} \\ F_y^t = F_{yj}^{tR} + F_{yj}^{tP} \\ F_z^t = F_{zj}^{tR} + F_{zj}^{tP} + F_M \end{cases} \quad (15)$$

The cutting force acting on the workpiece can be obtained by transforming the cutting force in the cutter coordinates to the that in the workpiece coordinates.

$$\begin{cases} F_x^w = F_x^t \cdot \cos\theta_t + F_y^t \cdot \sin\theta_t \\ F_y^w = -F_y^t \cdot \sin\theta_t + F_y^t \cdot \cos\theta_t \\ F_z^w = F_z^t \end{cases} \quad (16)$$

2.2.2 Modeling of the temperature distribution of the workpiece

Heat generation and heat transformed in the workpiece The heat generated in cutting mainly comes from three areas. In this paper, the temperature variation close to the machined area of the workpiece in CFRP orbital drilling is the focus; moreover, the powder chip has less friction with the rake face. Therefore, the effect of the tool-chip interface friction on the workpiece is not taken into account. Only the influence of the cutting heat from the primary and secondary heat sources on the workpiece is considered in this paper.

The heat generated during machining is mainly caused by the heat converted from cutting energy. The energy consumption of a cutting element in the first deformation zone can be calculated by Eq. (17). The shear velocity can be deduced from the relationship between the cutting speed and tool angles.

$$\dot{Q}_{fs}(\varphi) = F_s(\varphi) v_s \quad (17)$$

$$v_s = \frac{V \cos\gamma_n}{\cos\left(\phi_n - \gamma_n\right)} \quad (18)$$

The heat generated on the shear plane is divided into two parts. The part transferred to the workpiece can be calculated with the method in Ref. [52],

$$\dot{Q}_{fsw} = C_1 \dot{Q}_{fs} \quad (19)$$

where C_1 is the proportion of heat transferred to the workpiece to that generated in the first deformation zone. According to Shaw's [53] research, this proportion can be calculated by

$$C_1 = 1 - \frac{1}{1 + 1.328\sqrt{K_w \varepsilon / v_s h_j(\varphi)}} \quad (20)$$

where K_w is the thermal diffusivity of the workpiece and ε is the strain in the chip, which can be expressed as $\varepsilon = cot\,\varphi_n + tan\,(\varphi_n - \gamma_n)$.

The heat flux of a cutting element in the third deformation zone can be expressed as

$$\dot{Q}_{tf}(\varphi) = F_f(\varphi)V \tag{21}$$

The heat generated by the friction on the flank face is similar to that generated by the shear plane. The part transferred to the workpiece can be expressed as

$$\dot{Q}_{tfw} = C_2\dot{Q}_{tf} \tag{22}$$

where C_2 is the ratio of the heat transfer to the workpiece to the heat generated in the third deformation zone. According to Ref. [54], this proportion can be calculated by

$$C_2 = 1-\left(1+\frac{\pi K_w}{2h_j(\varphi)V\ln\frac{2b}{l_{wf}}}\right)^{-1} \tag{23}$$

Then, the heat flux transferred to the workpiece generated by a cutting element within one revolution can be expressed as follows:

$$q_{re} = \int_0^{2\pi}\left(g\left(\varphi_j\right)\left(C_1F_s(\varphi)v_s + C_2F_f(\varphi)V\right)\right)d\varphi \tag{24}$$

Analysis of the heat transfer in the workpiece The heat transfer in CFRP is relatively complex because the thermal conductivities in different directions are different. The short processing time and the heat accumulated in the workpiece induce an unsteady state, which makes it more difficult to predict the temperature of orbital drilling in CFRP. Therefore, most models of the temperature field for milling or grinding are not suitable for predicting the temperature field of orbital drilling on CFRP. A three-dimensional, unsteady state heat transfer equation considering convective heat transfer is established in this paper. To obtain the variation in the magnitude and distribution of workpiece temperatures, the finite difference method is used to solve the heat conduction equation. When the equation is solved with the finite difference method, it is necessary to approximate the shape of the hole wall with nodes. The application of polar coordinates in the calculation is conducive to the accuracy of the mathematics and the realization of the model calculations. This is more consistent with the physical process of heat diffusion. Therefore, the heat transfer equation in polar coordinates, which is used to calculate the temperature field distribution of orbital drilling of CFRP, is presented in Eqs. (25)-(27).

$$\lambda_1\frac{\partial^2T}{\partial r^2} + \lambda_1\frac{1}{r_w}\frac{\partial T}{\partial r} + \lambda_2\frac{1}{{r_w}^2}\frac{\partial^2T}{\partial\theta^2} + \lambda_3\frac{\partial^2T}{\partial z^2} + q(r_w,\theta_w,\mathrm{z}_w,\mathrm{t}) = \rho c\frac{\partial T}{\partial t} \tag{25}$$

The initial conditions are as follows:

$$T = T_0 \tag{26}$$

The boundary conditions are as follows:

$$-\lambda_1\frac{\partial T}{\partial n} = h(T-T_0) \tag{27}$$

where $q(r_w\theta_w z_w t)$ is the heat flux generated by the heat source. The heat conductivities in the x-, y-, and z-directions of unidirectional prepreg are different. Multidirectional CFRP is studied in this paper to simplify the calculation process, assuming that the heat conductivity of the workpiece in the y-direction is the same as that in the x-direction. From Eqs. (25)–(27), the heat transfer problem can be treated as a workpiece with different heat conductivities in the horizontal and vertical directions being placed in an environment with temperature T_0. Approximations are made, as shown in Eqs. (28) and (29), to rewrite the partial differential equation in finite difference form. The position of each node in the meshing of the workpiece is shown in Fig. 3.

$$\frac{\partial T}{\partial t} = \frac{T(i,j,k,t+1)-T(i,j,k,t)}{\Delta t} \tag{28}$$

$$\begin{aligned}
&\frac{1}{r_w}\frac{\partial T}{\partial r} = \frac{1}{2r_w\Delta r}(T(i+1,j,k)-T(i-1,j,k))\\
&\frac{\partial^2T}{\partial r^2} = \frac{1}{\Delta r^2}(T(i+1,j,k)+T(i-1,\mathrm{j},\mathrm{k})-2T(i,j,k))\\
&\frac{1}{{r_w}^2}\frac{\partial^2T}{\partial\theta^2} = \frac{1}{{r_w}^2\Delta\theta^2}(T(i,j+1,k)+T(i,j-1,k)-2T(i,j,k))\\
&\frac{\partial^2T}{\partial z^2} = \frac{1}{\Delta z^2}(T(i,j,k-1)+T(i,j,k+1)-2T(i,j,k))
\end{aligned} \tag{29}$$

It can be observed from Eqs. (17) to (21) that the energy consumption of a cutting element in the cutting process can be calculated by the cutting force and cutting speed. The heat flux produced by the element in steady cutting is a periodic function of the rotation angle. Therefore, the heat transfer process of milling and grinding can be regarded as the heat transfer process caused by a heat source with a fixed shape moving along the tool path.

However, in orbital drilling, cutting heat is generated by both the bottom edge and peripheral cutting edge, and the heat transfer process is more complex when the tool moves along a helical path. It is difficult to simulate the heat conduction

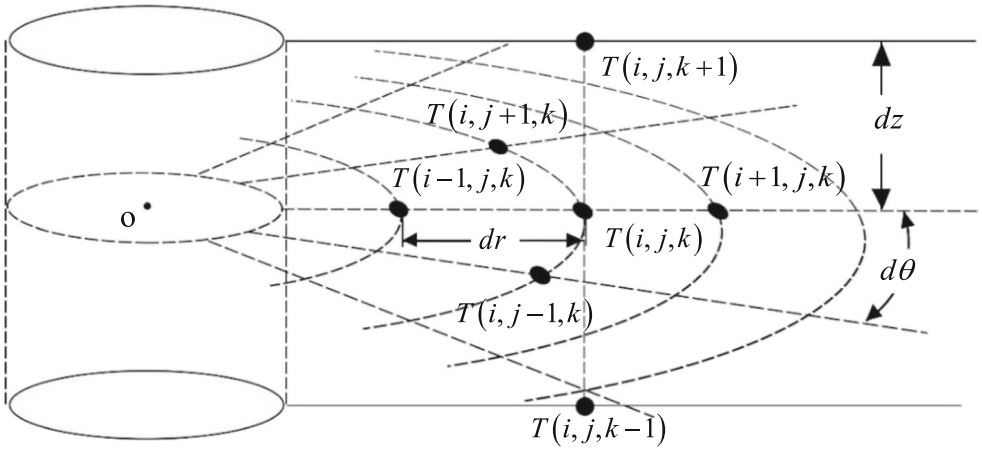

Fig. 3 Diagram of the workpiece meshing

process of orbital drilling with a simple moving heat source, and it is too difficult to obtain the solution.

The contact area between the ODR tool and the workpiece during steady cutting is shown in Fig. 2b and c. Equation 10 shows that the influence of the cutting edge rotation angle on the chip thickness is more significant than that of the tool radius. According to Eq. (24), the heat flux generated by the cutting element during processing is related to the rotation angle (φ) and the height (z) of the cutting element but not to the position of the tool. That is, the shape and heat distribution of the heat source formed on the cutting tool remain constant. Therefore, the heat transfer problem of orbital drilling can be treated as a complex curved surface heat source moving along a helical path in the workpiece, having the same shape as the contact area between the tool and the workpiece. Heat transfer occurs between the nodes inside the workpiece and the moving heat source. The material through which the heat source passes is removed, assuming that the temperature of the nodes

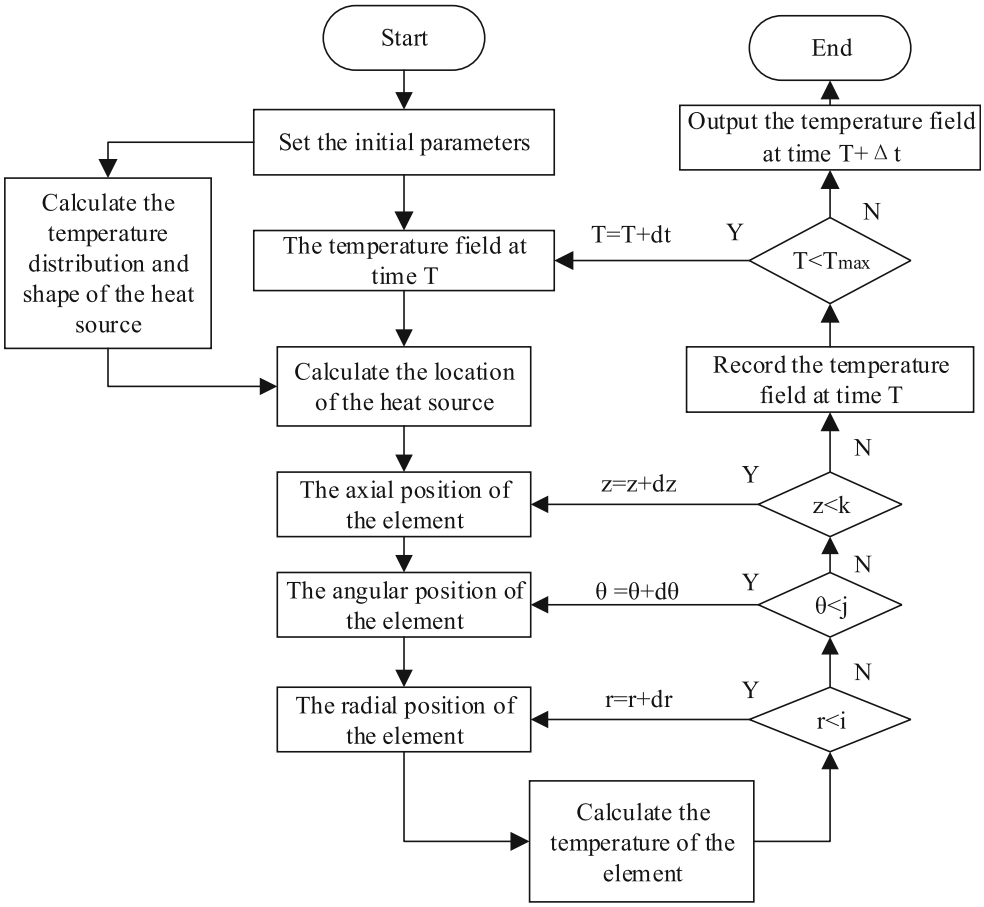

Fig. 4 A flow chart of the temperature field calculation

Table 1 Parameters of the tools and the workpiece

	Feature	Value
General end mill	Tool diameter	8 mm
	Carbides	K20
	Helix angle	30°
	Coating	No
	Flutes	4
	Rake angle of the end teeth and peripheral cutting edges	7°
	Tool clearance of the end teeth and peripheral cutting edges	7°
ODR tool	Diameter of the milling part	5.5 mm
	Diameter of the peripheral cutting edges	8 mm
	Radius of the arc of the ODR tool	10.625 mm
	Height of the reaming part	5 mm
	Carbide	K20
	Helix angle	30°
	Coating	No
	Flutes	4
	Rake angle of the milling part, reaming part and peripheral cutting edges	7°
	Tool clearance of the milling part, reaming part, and peripheral cutting edges	7°
Workpiece	Tensile strength	2400 MPa
	Young's modulus	160 GPa
	Heat conductivity of the workpiece in the x-direction	λ_1=4.18 $W\cdot(m\cdot K)^{-1}$
	Heat conductivity of the workpiece in the y-direction	λ_2=4.18 $W\cdot(m\cdot K)^{-1}$
	Heat conductivity of the workpiece in the z-direction	λ_3=0.76 $W\cdot(m\cdot K)^{-1}$
	Heat capacity of the workpiece	c_c=990 $J\cdot(kg\cdot K)^{-1}$
	Density of the workpiece	ρ=1520 $kg\cdot m^{-3}$
	Convective heat transfer coefficient	h=75 $W\cdot(m^2\cdot K)^{-1}$

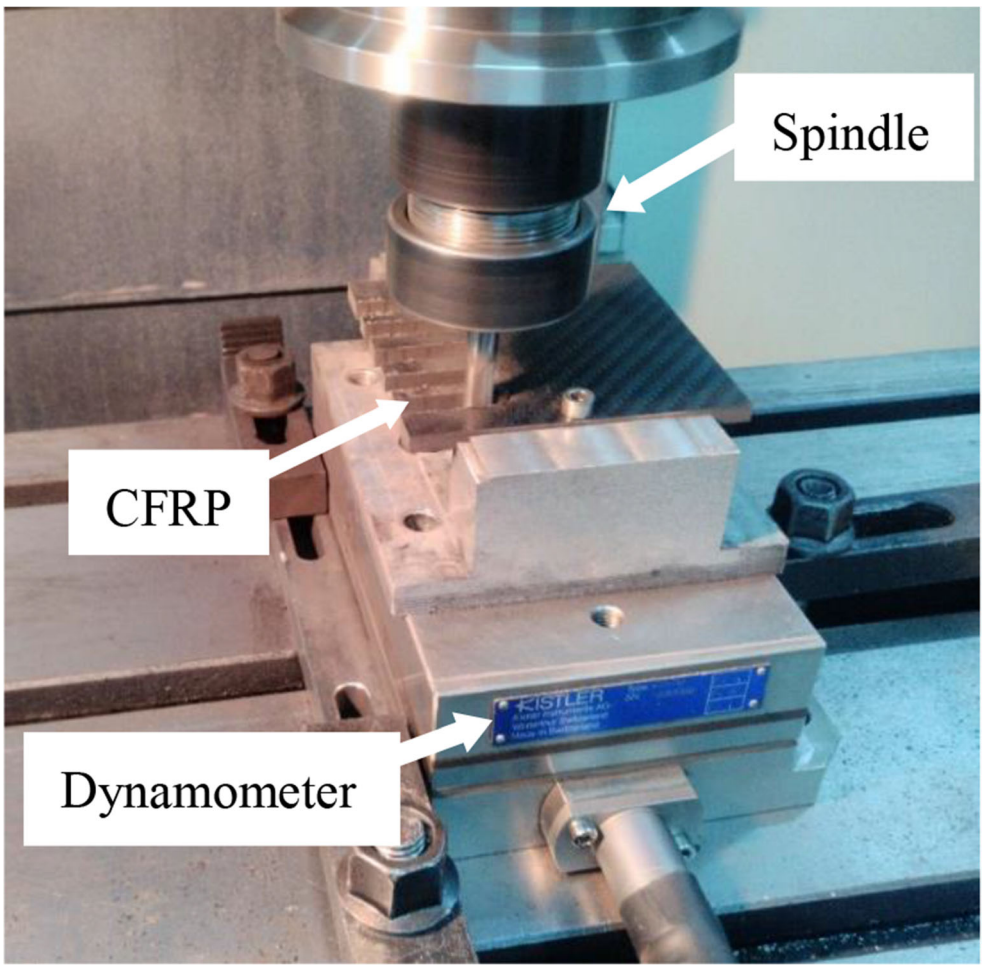

Fig. 5 The experimental setup in the cutting force coefficient identification experiment

Table 2 The experimental parameters

		Spindle speed (rpm)	Cutting depth a_p(mm)	Cutting diameter (mm)	Eccentricity (mm)	Tangential feed rate (mm/rev)	Z-axis feed rate (mm/rev)
Flank milling tests		1000	5			0.01, 0.02, 0.04, 0.08	
Plunge milling tests		1000		2, 3, 4, 5, 6, 7, 8			0.01, 0.02, 0.04, 0.08
Cutting force verification experiment		1000			1	0.126	0.02
Temperature distribution verification experiment	I	1000	1		1	0.063	0.01
	II	1500	0.5		1	0.063	0.005

that the heat source passes through becomes the ambient temperature, and convects heat with the newly formed boundary.

The calculation process of the temperature field is shown in Fig. 4.

3 Experimental work

3.1 Properties of the cutting tools and workpiece

To verify the usability of the cutting force model and the heat transfer model, a series of cutting tests were carried out with dedicated tools and general end mills. The workpiece was a multidirectional CFRP plate made from 3-k plain unidirectional prepreg with epoxy resin as the matrix material. After compression molding and high-temperature curing, the workpiece, which had two plies of woven prepreg as the top and bottom and 36 unidirectional plies with a symmetrical layout [0°, +45°, 90°, 45°] as the middleware, was cut into 90 mm×90 mm×5 mm pieces. The parameters of the tools and the workpiece in the experiments are listed in Table 1.

3.2 Design of experiments

The cutting force coefficients were demarcated according to the methods in Ref. [55]. The modeling process of the cutting

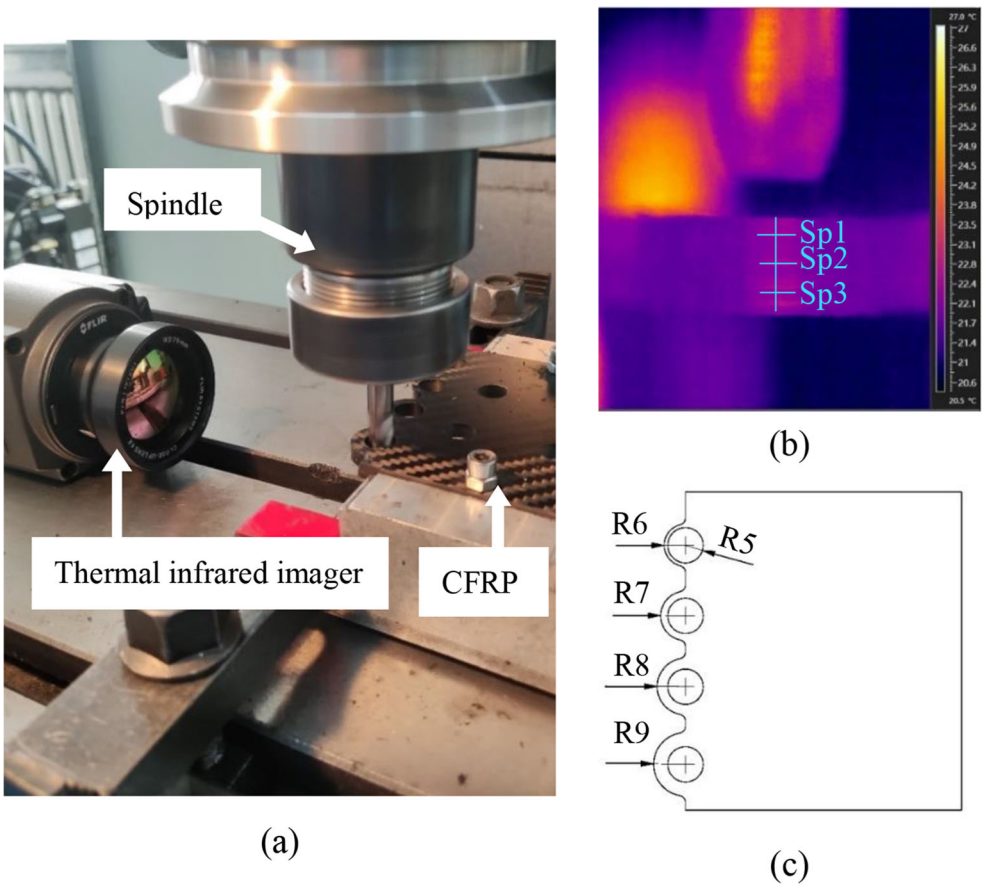

Fig. 6 **a** Experimental setup in test 2 and **b** infrared image of the workpiece. **c** The workpiece in the verification experiment of the temperature distribution model

Table 3 Cutting force coefficients

Reaming part	K_{tc}	K_{te}	K_{rc}	K_{re}	K_{ac}	K_{ae}
	636.00	3.74	735.90	11.65	-134.99	0.76
Peripheral cutting edges	K_{ptc}	K_{pte}	K_{prc}	K_{pre}	K_{pac}	K_{pae}
	580.50	5.02	866.40	13.32	-220.38	-0.99
Milling part	K_{mac}			K_{mae}		
	$269.90\times D_t$			$16.93\times D_t$		

force in orbital drilling is similar to that of milling, difference in the cutting force model being that the cutting edge involved in processing is more complex and that the cutting force needs to be transformed into workpiece coordinates in the end. According to Ref. [56], the cutting force coefficients of different parts in the tool were acquired. The cutting force coefficients of the reaming part and the peripheral cutting edge can be obtained in flank milling tests, and the coefficients of the milling part in the ODR tool and end mill can be obtained in plunge milling tests. The experiments were carried out on a VM7032 CNC milling machine, and a Kistler 9257B dynamometer and Kistler 5070 amplifier were used to measure and record the cutting force. The experimental setup is shown in Fig. 5. The experimental parameters of the flank milling tests, plunge milling tests, and verification experiment are listed in Table 2.

To verify the validity of the temperature distribution model, a verification experiment was carried out. To measure the cutting temperature at the hole wall during machining, a FLIR A320 Tempscreen thermal infrared imager and a close-up lens 4× were used in the test. The experimental setups are illustrated in Fig. 6. To facilitate thermal imaging and to avoid the influence of uneven material thickness, semicircles with radii of 6 mm, 7 mm, 8 mm, and 9 mm around the hole for predicting different material thicknesses were made on the workpiece to verify the accuracy of the model in different cutting parameters. The cutting conditions are listed in Table 2. To prevent chips from blocking the imaging, flowing air was used to remove the chips, and all the experiments adopted dry machining.

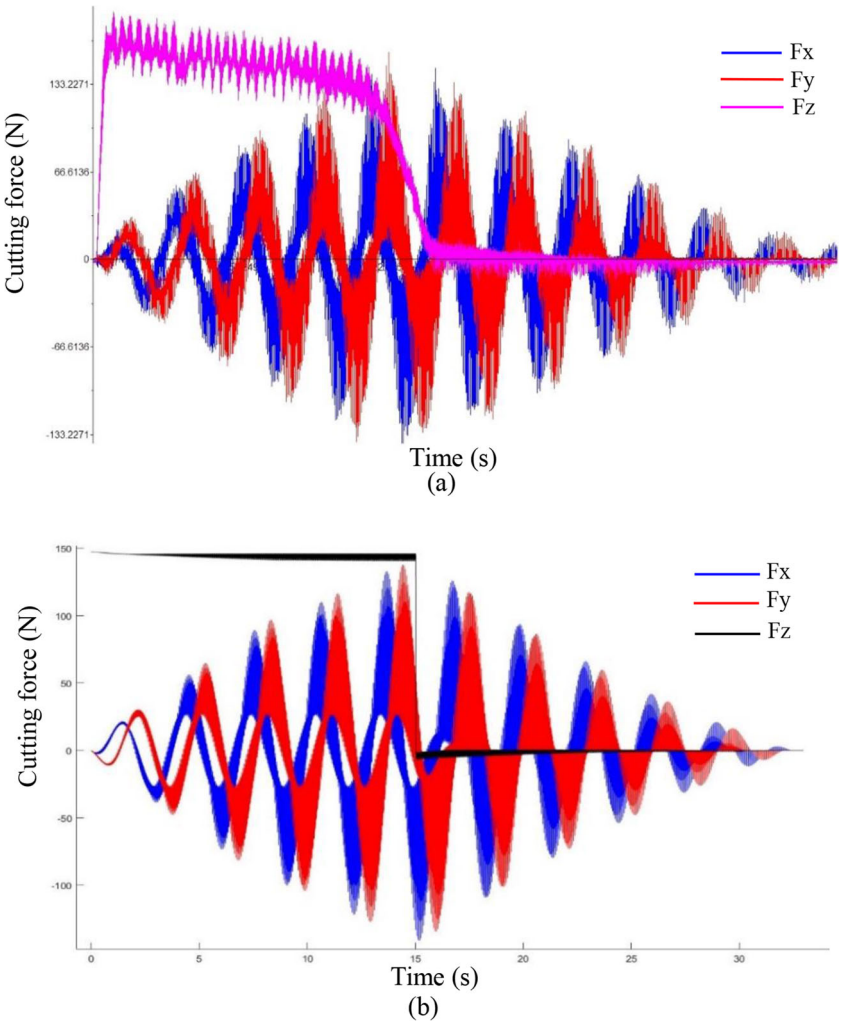

Fig. 7 Predictions and experimental results: **a** experimental results, **b** predictions of the cutting force model

4 Results and discussion

4.1 Verification of the cutting force model

To predict the cutting force of orbital drilling with the ODR tool, a cutting force coefficient identification experiment was carried out. The coefficients of the cutting edges in the reaming part and the peripheral cutting edges were identified with the method in Ref. [57], and the coefficients of the cutting edges in the milling part were identified with the method in Refs. [56, 58]. The average cutting force in steady cutting was used to identify the cutting force coefficient, and the coefficient of the ODR tool is listed in Table 3. The end mill employed in this research had the same parameters as the ODR tool, assuming that the end mill had the same cutting force coefficient as the peripheral cutting edges and the edges on the milling part of the ODR tool.

As can be observed in Table 3, the cutting force coefficients K_{pac} and K_{pae} are negative, which means that the thrust force generated by the cutting edges on the peripheral cutting edges of an end mill and an ODR tool is directed upward. The cutting force coefficient K_{ac} is negative, and K_{ae} is positive, which means that the direction of the thrust force generated by the cutting edges of the reaming part is affected by the cutting parameters. The thrust force generated by the reaming part is positive when the tangential feed per tooth is small. The thrust force gradually decreases to a negative value with increasing tangential feed rate, and the direction changes. Therefore, the thrust force in orbital drilling is almost completely produced by the edges at the bottom of the end mill and the ODR tool. The magnitude of the thrust force is positively correlated with the diameter of the cutting edges at the bottom. The predictions of the cutting force model and the experimental results of ODR are shown in Fig. 7.

As can be observed in Fig. 7a, at the beginning of machining, the thrust force soars to the maximum value, and the cutting force in the x- and y-directions is affected by the planetary motion of the tool, which changes periodically. The cutting force increases gradually while the reaming part penetrates the workpiece, and the cutting force in the x- and y-directions reach the maximum when the reaming part completely enters the workpiece. The thrust force decreases rapidly to zero when the milling part passes through the bottom of the workpiece, and the cutting forces in the x- and y-directions begin to decrease gradually. As presented in Fig. 7b, the predictions of the model are consistent with the experimental results. The cutting force model can accurately predict the magnitude and trend of the cutting force in the x-, y-, and z-directions. However, the model cannot show that the thrust force decreases with increasing machining depth, probably due to workpiece deformation. The same prediction result is obtained from orbital drilling with the end mill. The results show that the model can be used to predict the cutting force of the end mill and the ODR tool in orbital drilling.

4.2 Verification of the temperature distribution model

In the verification of the heat transfer model, first, the heat fluxes generated by two kinds of cutting tools were calculated under the experimental conditions (an eccentricity of 1 mm, a tangential feed rate of v_{ft} = 0.063 mm/rev, a Z-axis feed rate of v_{fa} = 0.01 mm/rev, and a tool rotational speed of 1000 rpm).

The heat generated by peripheral cutting edges and the edges of the reaming part directly acts on the hole wall and has the most apparent effect on the temperature. Therefore, the heat fluxes produced by the peripheral cutting edge and the edge on the reaming part of the two kinds of tools are shown in Fig. 8. The heat fluxes generated by a cutting edge of the end mill in a cycle, with the hole wall formed at the top of the workpiece when the cutter first contacts the workpiece as an example, are marked by a red line. According to the cutting parameters, the materials composing the hole wall are cut six times by the ODR tool, and the heat fluxes and the action times are depicted in blue.

Figure 8 shows that the cutting edge of an end mill generates heat between 0° and 180° in a rotational period and that the heat flux changes as a sine function due to the influence of

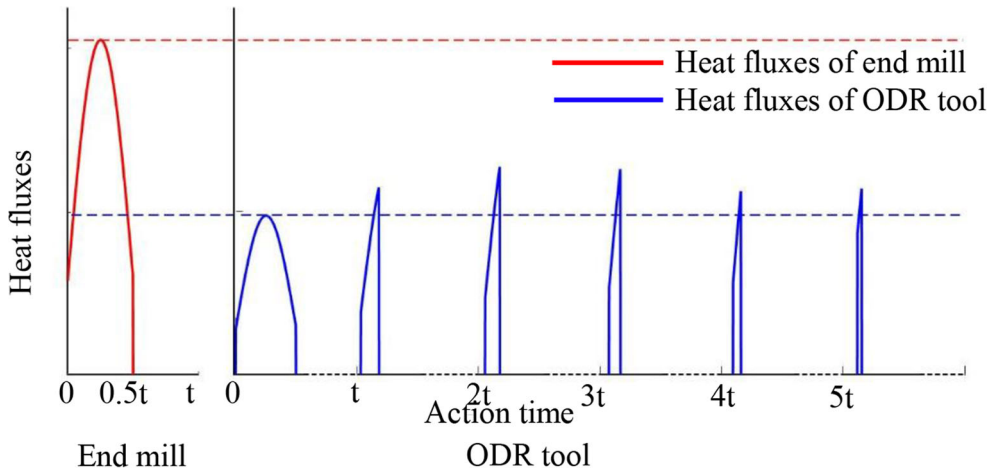

Fig. 8 Heat fluxes of the peripheral cutting edge and the edge on the reaming part of two kinds of tools

the chip thickness. In the first cutting revolution, the heat flux generated by the cutting edge of the ODR tool exhibits the same trend as that of the end mill, and the heat fluxes are lower than that of the end mill due to the low cutting speed. The maximum value of the heat flux increases in the 2nd to 6th machining cycle due to the increase in the tool radius and the change in the chip thickness. However, affected by the undeformed chip geometry, the action time decreases gradually. The total heat flux generated by the ODR cutter is less than that of the end mill, and the ODR tool disperses the heat in multiple processing revolutions and gradually acts on the workpiece, making full use of the heat dissipation process in each processing revolution to reduce the temperature of the workpiece.

In this paper, the calculated results of the heat transfer model are compared with the experimental results measured by an infrared thermal imager. The results are shown in Fig. 9.

The graphs in Fig. 9 show comparisons of the simulation and experimental results for the machining temperature at different marked points on the ODR tool and the end mill. As presented in Fig. 9, the ODR tool has lower cutting temperatures at every marked point. Owing to the multiple expansions by the reaming part, the processing revolutions of the ODR

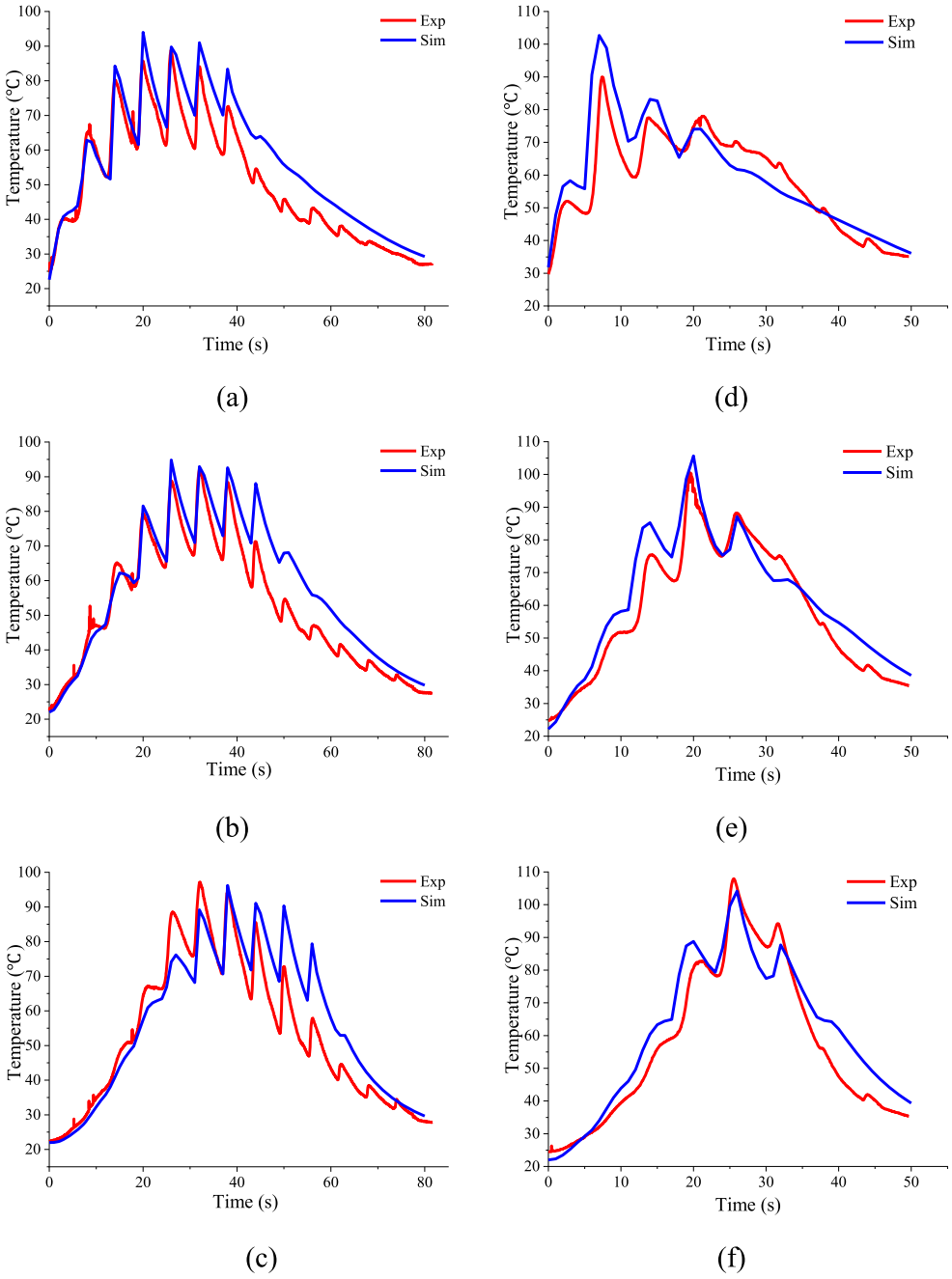

Fig. 9 Comparison of simulation results and experimental results of machining temperature: **a** results comparison for ODR at location sp1, **b** results comparison for ODR at location sp2, **c** results comparison for ODR at location sp3, **d** results comparison for end mill at location sp1, **e** results comparison for end mill at location sp2, and **f** results comparison for end mill at sp3

tool at each point are much greater than those of the end mill, and the temperature increase produced by each revolution of ODR is significantly lower than that of the end mill. The workpiece temperature accumulation of the end mill is much more obvious than that of the ODR tool. As observed from Fig. 9c and f, the highest cutting temperature appears at the marked points near the bottom for both kinds of tools. The comparison of the simulation and experimental results shows that the temperature distribution model can predict the change in the workpiece temperature field during machining. However, as presented in Fig. 9a–f, there are no obvious distinctions among the maximum temperatures of the three marked points, probably because the temperature distribution model, which takes the heat flux generated by the tool during steady cutting as the moving heat source, ignores the temperature change of the tool in the machining process. The temperature distribution model does not take the heat generated after machining by the friction between the cutting edge and the machined surface into account; therefore, the serrated temperature fluctuations in the last stage are not presented in the graphs in Fig. 9. The simulation results and the experimental results show that the processing temperature of the marked point near the bottom of the workpiece is the highest, and this high processing temperature easily causes defects, which is consistent with defects always being present at the hole exit. Figure 10 shows the experimental and simulation results for the sp3 temperature from two groups of tests for the ODR tool and end mill at different material thicknesses.

As observed from Fig. 10, when processing with the same cutting parameters, the cutting temperature of the end mill is higher than that of ODR. The temperature of the material close to the hole wall is the highest in the horizontal direction, and the temperature of the marked point decreases gradually with increasing material thickness. Therefore, the matrix near the hole wall is prone to melting. As can be observed from Fig. 10a–d, the experimental results exhibit the same trend as the simulation results. Although the temperature distribution model cannot accurately predict the processing temperature, the errors between the predicted results and the experimental results are mostly less than 15%.

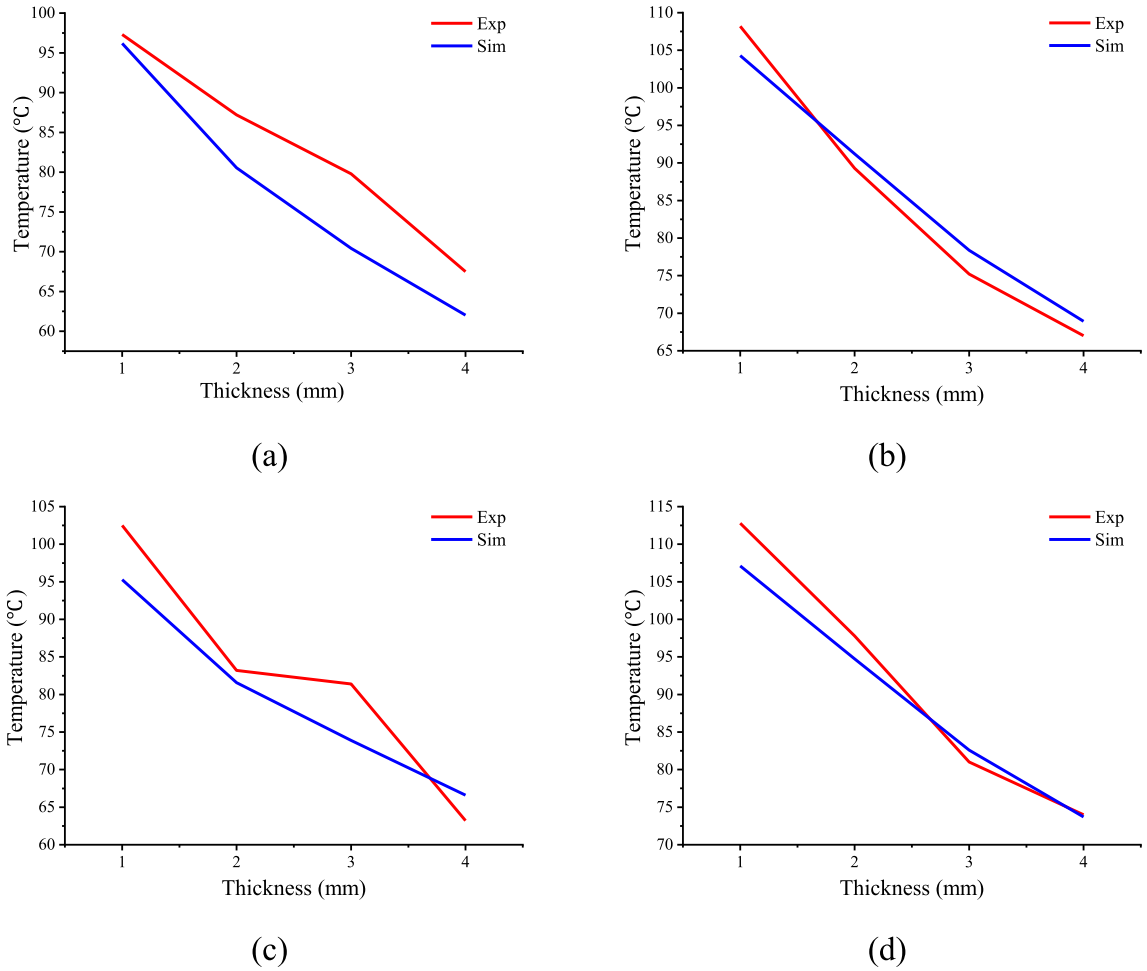

Fig. 10 Maximum processing temperature of the experimental results and simulation results: **a** results for the ODR tool under cutting condition I, **b** results for the end mill under cutting condition I, **c** results for the ODR tool under cutting condition II, and **d** results for the end mill under cutting condition II

5 Conclusion

In this paper, the cutting temperature of orbital drilling in CFRP with two kinds of tools was studied. A numerical model solved by the finite difference method was used to predict the heat conduction process. The proposed temperature distribution model is capable of representing the changing temperature field inside the workpiece. The following conclusions are made:

1. For end mill and ODR tools, the thrust force is generated by the cutting edge at the bottom of the tool, and the thrust force generated by the peripheral cutting edge and the edge on the reaming part is directed upward in orbital drilling.
2. The total heat generated by the ODR tool is lower than that generated by the end mill, and the processing temperature of the ODR tool is lower than that of the end mill.
3. The temperature distribution model can be utilized for predicting the cutting temperature inside the workpiece during orbital drilling of CFRP. The finite difference method can be used to obtain the solutions of the heat transfer equation, and errors in the result compared with the experimental results are small.
4. During machining, the processing temperature near the exit of the hole wall is higher than that near the entrance. The temperature of the material near the hole wall inside the workpiece is higher, and the temperature gradually decreases with increasing distance.

Code availability Not applicable.

Author contribution LHK, YL, and DG conceived and designed the study. LHK performed the experiments. LHK wrote the paper. LHK, YL, and DG reviewed and edited the manuscript. All authors read and approved the manuscript.

Funding The authors received financial support from the National Key Research and Development Program of China under Grant No. 2019YFB1704803.

Data availability All data are fully available without restriction.

Declarations

Conflict of interest The authors declare no competing interests.

References

1. Gao YF, Xiong J, Xiao JH, Lu D (2019) A tilted orbital grinding technique for hole-making of CFRP composite laminates. Int J Adv Manuf Technol 104(1-4):661–673. https://doi.org/10.1007/s00170-019-03904-x
2. Wang CY, Chen YH, An QL, Cai XJ, Ming WW, Chen M (2015) Drilling temperature and hole quality in drilling of CFRP/aluminum stacks using diamond coated drill. Int J Precis Eng Manuf 16(8):1689–1697. https://doi.org/10.1007/s12541-015-0222-y
3. Ben W, Hang G, Quan W, Maoqing W, Songpeng Z (2012) Influence of cutting heat on quality of drilling of carbon/epoxy composites. Mater Manuf Process 27(9):968–972. https://doi.org/10.1080/10426914.2011.610079
4. Bonnet C, Poulachon G, Rech J, Girard Y, Costes JP (2015) CFRP drilling: Fundamental study of local feed force and consequences on hole exit damage. Int J Mach Tool Manu 94:57–64. https://doi.org/10.1016/j.ijmachtools.2015.04.006
5. Feito N, Diaz-Alvarez J, Lopez-Puente J, Miguelez MH (2018) Experimental and numerical analysis of step drill bit performance when drilling woven CFRPs. Compos Struct 184:1147–1155. https://doi.org/10.1016/j.compstruct.2017.10.061
6. Durao LMP, Goncalves DJS, Tavares JMRS, de Albuquerque VHC, Vieira AA, Marques AT (2010) Drilling tool geometry evaluation for reinforced composite laminates. Compos Struct 92(7):1545–1550. https://doi.org/10.1016/j.compstruct.2009.10.035
7. Su F, Zheng L, Sun FJ, Wang ZH, Deng ZH, Qiu XY (2018) Novel drill bit based on the step-control scheme for reducing the CFRP delamination. J Mater Process Technol 262:157–167. https://doi.org/10.1016/j.jmatprotec.2018.06.037
8. Isbilir O, Ghassemieh E (2013) Numerical investigation of the effects of drill geometry on drilling induced delamination of carbon fiber reinforced composites. Compos Struct 105:126–133. https://doi.org/10.1016/j.compstruct.2013.04.026
9. Qiu XY, Li PN, Niu QL, Chen AH, Ouyang PR, Li CP, Ko TJ (2018) Influence of machining parameters and tool structure on cutting force and hole wall damage in drilling CFRP with stepped drills. Int J Adv Manuf Technol 97(1-4):857–865. https://doi.org/10.1007/s00170-018-1981-2
10. Butler-Smith PW, Axinte DA, Dame M, Kennedy AR, Harper LT, Bucourt JF, Ragueneau R (2015) A study of an improved cutting mechanism of composite materials using novel design of diamond micro-core drills. Int J Mach Tool Manu 88:175–183. https://doi.org/10.1016/j.ijmachtools.2014.10.002
11. Hocheng H, Tsao CC (2005) The path towards delamination-free drilling of composite materials. J Mater Process Technol 167(2-3):251–264. https://doi.org/10.1016/j.jmatprotec.2005.06.039
12. Qiu XY, Li PN, Li CP, Niu QL, Chen AH, Ouyang PR, Ko TJ (2018) Study on chisel edge drilling behavior and step drill structure on delamination in drilling CFRP. Compos Struct 203:404–413. https://doi.org/10.1016/j.compstruct.2018.07.007
13. Tsao CC (2008) Experimental study of drilling composite materials with step-core drill. Mater Des 29(9):1740–1744. https://doi.org/10.1016/j.matdes.2008.03.022
14. Zimmermann M, Heberger L, Schneider F, Effgen C, Aurich JC (2016) Investigation of chip formation and workpiece load when machining carbon-fiber-reinforced-polymer (CFRP). 16th Machining Innovations Conference for Aerospace Industry - Mic 2016 6:124-131. doi:https://doi.org/10.1016/j.promfg.2016.11.016
15. Shyha IS, Aspinwall DK, Soo SL, Bradley S (2009) Drill geometry and operating effects when cutting small diameter holes in CFRP. Int J Mach Tool Manu 49(12-13):1008–1014. https://doi.org/10.1016/j.ijmachtools.2009.05.009
16. Iliescu D, Gehin D, Gutierrez ME, Girot F (2010) Modeling and tool wear in drilling of CFRP. Int J Mach Tool Manu 50(2):204–213. https://doi.org/10.1016/j.ijmachtools.2009.10.004
17. Pereira RBD, Brandao LC, de Paiva AP, Ferreira JR, Davim JP (2017) A review of helical milling process. Int J Mach Tool Manu 120:27–48. https://doi.org/10.1016/j.ijmachtools.2017.05.002
18. Brinksmeier E, Fangmann S, Meyer I (2008) Orbital drilling kinematics. Prod Eng 2(3):277–283. https://doi.org/10.1007/s11740-008-0111-7

19. Geier N, Davim JP, Szalay T (2019) Advanced cutting tools and technologies for drilling carbon fibre reinforced polymer (CFRP) composites: a review. Compos Part a-Appl S 125:105552. https://doi.org/10.1016/j.compositesa.2019.105552
20. Pereszlai C, Geier N (2020) Comparative analysis of wobble milling, helical milling and conventional drilling of CFRPs. Int J Adv Manuf Technol 106(9-10):3913–3930. https://doi.org/10.1007/s00170-019-04842-4
21. Xu WX, Zhang LC (2014) On the mechanics and material removal mechanisms of vibration-assisted cutting of unidirectional fibre-reinforced polymer composites. Int J Mach Tool Manu 80-81:1–10. https://doi.org/10.1016/j.ijmachtools.2014.02.004
22. Alberdi A, Suarez A, Artaza T, Escobar-Palafox GA, Ridgway K (2013) Composite Cutting with abrasive water jet. Manuf Eng Soc Int Conf, (Mesic 2013) 63:421–429. https://doi.org/10.1016/j.proeng.2013.08.217
23. Herzog D, Jaeschke P, Meier O, Haferkamp H (2008) Investigations on the thermal effect caused by laser cutting with respect to static strength of CFRP. Int J Mach Tool Manu 48(12-13):1464–1473. https://doi.org/10.1016/j.ijmachtools.2008.04.007
24. Teicher U, Muller S, Munzner J, Nestler A (2013) Micro-EDM of carbon fibre-reinforced plastics. Proc Seventeenth Cirp Conf Electro Physical Chem Mach (Isem) 6:320–325. https://doi.org/10.1016/j.procir.2013.03.092
25. Wang Q, Wu Y, Bitou T, Nomura M, Fujii T (2017) Proposal of a tilted helical milling technique for high quality hole drilling of CFRP: kinetic analysis of hole formation and material removal. Int J Adv Manuf Technol 94(9-12):4221–4235. https://doi.org/10.1007/s00170-017-1106-3
26. Voss R, Henerichs M, Kuster F (2016) Comparison of conventional drilling and orbital drilling in machining carbon fibre reinforced plastics (CFRP). Cirp Ann-Manuf Technol 65(1):137–140. https://doi.org/10.1016/j.cirp.2016.04.001
27. Wang GD, Kirwa MS, Li N (2018) Experimental studies on a two-step technique to reduce delamination damage during milling of large diameter holes in CFRP/Al stack. Compos Struct 188:330–339. https://doi.org/10.1016/j.compstruct.2018.01.039
28. Taylor FW (1907) The art of cutting metals. Sci Am 63(1618supp): 25929–25931
29. Komanduri R, Hou ZB (2000) Thermal modeling of the metal cutting process - Part I - temperature rise distribution due to shear plane heat source. Int J Mech Sci 42(9):1715–1752. https://doi.org/10.1016/S0020-7403(99)00070-3
30. Komanduri R, Hou ZB (2001) Thermal modeling of the metal cutting process — Part II: temperature rise distribution due to frictional heat source at the tool–chip interface. Int J Mech Sci 43(1): 57–88. https://doi.org/10.1016/s0020-7403(99)00104-6
31. Komanduri R, Hou ZB (2001) Thermal modeling of the metal cutting process — Part III: temperature rise distribution due to the combined effects of shear plane heat source and the tool–chip interface frictional heat source. Int J Mech Sci 43(1):89–107. https://doi.org/10.1016/s0020-7403(99)00105-8
32. Lin S, Peng FY, Wen J, Liu YZ, Yan R (2013) An investigation of workpiece temperature variation in end milling considering flank rubbing effect. Int J Mach Tool Manu 73:71–86. https://doi.org/10.1016/j.ijmachtools.2013.05.010
33. Huang Y, Liang SY (2005) Cutting temperature modeling based on non-uniform heat intensity and partition ratio. Mach Sci Technol 9(3):301–323. https://doi.org/10.1080/10910340500196421
34. Bäker M (2006) Finite element simulation of high-speed cutting forces. J Mater Process Technol 176(1-3):117–126. https://doi.org/10.1016/j.jmatprotec.2006.02.019
35. Li R, Shih AJ (2005) Finite element modeling of 3D turning of titanium. Int J Adv Manuf Technol 29(3-4):253–261. https://doi.org/10.1007/s00170-005-2511-6
36. Umbrello D, M'Saoubi R, Outeiro JC (2007) The influence of Johnson–Cook material constants on finite element simulation of machining of AISI 316L steel. Int J Mach Tools Manuf 47(3-4): 462–470. https://doi.org/10.1016/j.ijmachtools.2006.06.006
37. Dutt RP, Brewer RC (1965) On the theoretical determination of the temperature field in orthogonal machining. Int J Prod Res 4(2):91–114. https://doi.org/10.1080/00207546508919968
38. Lazoglu I, Altintas Y (2002) Prediction of tool and chip temperature in continuous and interrupted machining. Int J Mach Tool Manu 42(9):1011–1022. https://doi.org/10.1016/S0890-6955(02)00039-1
39. Liu J, Ren CZ, Qin XD, Li H (2014) Prediction of heat transfer process in helical milling. Int J Adv Manuf Technol 72(5-8):693–705. https://doi.org/10.1007/s00170-014-5662-5
40. Liu J, Chen G, Ji CH, Qin XD, Li H, Ren CZ (2014) An investigation of workpiece temperature variation of helical milling for carbon fiber reinforced plastics (CFRP). Int J Mach Tool Manu 86:89–103. https://doi.org/10.1016/j.ijmachtools.2014.06.008
41. Zhang BY, Wang FJ, Wang XD, Li Y, Wang Q (2020) Optimized selection of process parameters based on reasonable control of axial force and hole-exit temperature in drilling of CFRP. Int J Adv Manuf Technol 110(3-4):797–812. https://doi.org/10.1007/s00170-020-05868-9
42. Sun Y, Sun J, Li J, Xiong Q (2013) An experimental investigation of the influence of cutting parameters on cutting temperature in milling Ti6Al4V by applying semi-artificial thermocouple. Int J Adv Manuf Technol 70(5-8):765–773. https://doi.org/10.1007/s00170-013-5294-1
43. Sheng J, Chiu Y-J, Lin B-J (2017) Determination of a coupling equation for milling parameters based on optimal cutting temperature. Int J Adv Manuf Technol 98(1-4):129–141. https://doi.org/10.1007/s00170-017-0542-4
44. Wang H, Sun J, Li J, Lu L, Li N (2015) Evaluation of cutting force and cutting temperature in milling carbon fiber-reinforced polymer composites. Int J Adv Manuf Technol 82(9-12):1517–1525. https://doi.org/10.1007/s00170-015-7479-2
45. Weinert K, Brinkel F, Kempmann C, Pantke K (2007) The dependency of material properties and process conditions on the cutting temperatures when drilling polymers. Prod Eng 1(4):381–387. https://doi.org/10.1007/s11740-007-0015-y
46. Guimarães B, Fernandes CM, Figueiredo D, Cerqueira MF, Carvalho O, Silva FS, Miranda G (2020) A novel approach to reduce in-service temperature in WC-Co cutting tools. Ceram Int 46(3):3002–3008. https://doi.org/10.1016/j.ceramint.2019.09.299
47. Sasahara H, Satake K, Takahashi W, Goto M, Yamamoto H (2017) The effect of oil mist supply on cutting point temperature and tool wear in driven rotary cutting. Precis Eng 48:158–163. https://doi.org/10.1016/j.precisioneng.2016.11.016
48. Merino-Perez JL, Royer R, Merson E, Lockwood A, Ayvar-Soberanis S, Marshall MB (2016) Influence of workpiece constituents and cutting speed on the cutting forces developed in the conventional drilling of CFRP composites. Compos Struct 140: 621–629. https://doi.org/10.1016/j.compstruct.2016.01.008
49. Yashiro T, Ogawa T, Sasahara H (2013) Temperature measurement of cutting tool and machined surface layer in milling of CFRP. Int J Mach Tool Manu 70:63–69. https://doi.org/10.1016/j.ijmachtools.2013.03.009
50. Chen T, Ye ML, Deng Y, Liu SL (2018) Study of temperature field for UVAG of CFRP based on FBG. Int J Adv Manuf Technol 96(1-4):765–773. https://doi.org/10.1007/s00170-018-1642-5
51. Kong L, Gao D, Lu Y, Jiang Z (2020) Novel orbital drilling and reaming tool for machining holes in carbon fiber–reinforced plastic (CFRP) composite laminates. Int J Adv Manuf Technol 110(3-4): 977–988. https://doi.org/10.1007/s00170-020-05928-0
52. Zhirong L (2017) Research on bone cutting and a novel tool development. Dissertation, Harbin Institute of Technology,

53. Shaw MC, Cookson JO (1985) Metal cutting principles. Tribol Int 18(1):55–55
54. Berliner EM, Krainov VP (1991) Analytic calculations of the temperature-field and heat flows on the tool surface in metal-cutting due to sliding friction. Wear 143(2):379–395. https://doi.org/10.1016/0043-1648(91)90108-7
55. Budak E, Altintas Y, Armarego EJA (1996) Prediction of milling force coefficients from orthogonal cutting data. J Manuf Sci E-T Asme 118(2):216–224. https://doi.org/10.1115/1.2831014
56. Denkena N, Rehe, & Dege. (2011) Process force prediction in orbital drilling of TiAl6V4. 9th International Conference on Advanced Manufacturing Systems and Technology
57. Wang MH, Gao L, Zheng YH (2014) An examination of the fundamental mechanics of cutting force coefficients. Int J Mach Tool Manu 78:1–7. https://doi.org/10.1016/j.ijmachtools.2013.10.008
58. Haiyan W, Xuda Q (2015) A mechanistic model for cutting force in helical milling of carbon fiber-reinforced polymers. Int J Adv Manuf Technol 82(9-12):1485–1494. https://doi.org/10.1007/s00170-015-7460-0

Publisher's note Springer Nature remains neutral with regard to jurisdictional claims in published maps and institutional affiliations.